

Disk formation in the collapse of supramassive neutron stars

Giovanni Camelio¹, Tim Dietrich^{2,3}, Stephan Rosswog¹

¹ *Astronomy and Oskar Klein Centre, Stockholm University, AlbaNova, SE-10691, Stockholm, Sweden*

² *Nikhef, Science Park, 1098 XG Amsterdam, The Netherlands*

³ *Max Planck Institute for Gravitational Physics (Albert Einstein Institute), Am Mühlenberg 1, Potsdam 14476, Germany*

14 December 2024

ABSTRACT

Short gamma-ray bursts (sGRBs) show a large diversity in their properties. This suggests that the observed phenomenon can be caused by different “central engines” or that the engine produces a variety of outcomes depending on the specific system parameters, or possibly both. The most popular engine scenario, the merger of two neutron stars, has received support from the recent Fermi detection of a burst of gamma rays (GRB170817A) following the neutron star merger GW170817, but at the moment it is not clear how peculiar this event potentially was. Several sGRBs engine models involve the collapse of a supramassive neutron star that produces a black hole plus an accretion disk. We study this scenario for a variety of equations of states both via angular momentum considerations based on equilibrium models and via fully dynamical Numerical Relativity simulations. We obtain a broader range of disk forming configurations than earlier studies but, in agreement with the latter, we find that none of these configurations is likely to produce a phenomenon that would be classified as an sGRB.

Key words: accretion discs, hydrodynamics, methods: numerical, stars: gamma-ray burst: general, stars: neutron, stars: rotation.

1 INTRODUCTION

With the first detection of a neutron star merger in both gravitational (Abbott et al. 2017a) and electromagnetic waves (Abbott et al. 2017c) the era of multi-messenger astrophysics has begun in earnest. This single event brought a major leap forward for a number of areas: it allowed for a new, independent measurement of the Hubble constant (Abbott et al. 2017b), it conclusively established that neutron star mergers are a major cosmic source of r-process elements (Lattimer & Schramm 1974; Eichler et al. 1989; Rosswog et al. 1999; Freiburghaus et al. 1999; Cowperthwaite et al. 2017; Smartt et al. 2017; Kasliwal et al. 2017; Kasen et al. 2017; Tanvir et al. 2017; Rosswog et al. 2017), and, with precise limits on the propagation speed of gravitational waves (Abbott et al. 2017c), it placed strict constraints on alternative theories of gravity. Moreover, the triggering of the FERMI satellite on a short gamma-ray burst (sGRB) 1.7 seconds after the gravitational wave (GW) peak lends support to the long-held conjecture that neutron star mergers produce GRBs (Paczynski 1986; Eichler et al. 1989). It is, however, an open question whether this GRB event was an intrinsically sub-luminous one with $E_{\gamma,\text{iso}} \sim 6 \times 10^{46}$ erg (Kasliwal et al. 2017; Mooley et al. 2018; Nakar et al. 2018) or a typical short GRB with $\sim 10^{50} - 10^{52}$ erg (Berger 2014;

Fong et al. 2015), but seen off axis, see for example Margutti et al. (2018).

In general, sGRBs exhibit a large variety of properties and it is not well understood how this diversity relates to the central engine(s). A particularly puzzling property is late-time X-ray activity on time scales that exceed the dynamical time scales of a compact engine (~ 1 ms) by many orders of magnitude, see e.g. Villaseñor et al. (2005); Barthelmy et al. (2005); Rowlinson et al. (2013); Gompertz et al. (2014). This led MacFadyen et al. (2005) to suggest that such bursts could be caused by neutron stars (NSs) accreting from a non-degenerate companion star. Upon collapse, a black hole (BH) plus accretion disk system would form and launch the relativistic outflow that produces the GRB. The late X-ray activity would result from the interaction of the outflow with the extended companion star. The accretion disk would need to have a mass of the order of

$$M_{\text{disk}} \sim 2 \times 10^{-4} M_{\odot} \left(\frac{E_{\text{iso}}}{10^{51} \text{ erg}} \right) \left(\frac{f_b}{1/50} \right) \left(\frac{0.05}{\varepsilon} \right), \quad (1)$$

where M_{disk} is the disk mass, ε is the accretion efficiency, $E_{\gamma,\text{iso}}$ is the GRB energy deduced from the observed luminosity assuming isotropic emission, and $f_b = \Delta\Omega/4\pi$ is the beaming fraction. The late X-ray activity is also addressed in so-called “time-reversal scenarios” (Ciolfi & Siegel 2015;

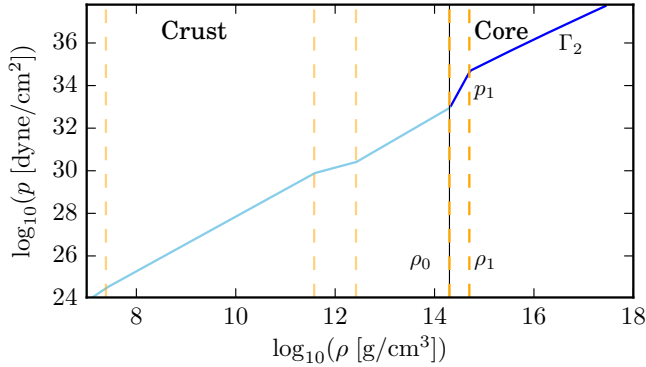


Figure 1. Example of the six-piece polytropic EOS employed in this work. The light blue line refers to the SLy crust employed at low densities, while the dark blue line refers to the high density part of the EOS. We mark the transition between the different polytropic pieces with dashed orange lines. The thin black vertical line corresponds to $\rho_0 = 10^{14.3} \text{ g/cm}^3$, namely the density at which the crust is attached to the high density EOS.

Rezzolla & Kumar 2015) where a long-lived supramassive neutron star produces the long-lasting X-ray emission which initially is trapped in an optically thick nebula. As in the scenario proposed by MacFadyen et al. (2005), also here it is crucial for the model that at some point the supramassive neutron star collapses to black hole plus torus system to launch the GRB.

The question whether such a collapse really produces an accretion torus that is massive enough for launching a typical sGRB, has recently been addressed by Margalit et al. (2015). They constructed rapidly rotating neutron stars using the RNS code (Stergioulas & Friedman 1995) and studied the corresponding angular momentum distribution. The authors came to the conclusion that it is unlikely that an accretion disk massive enough to launch an energetic GRB can be formed. In this paper, we revisit this problem. We construct our initial conditions with the XNS code (Bucciantini & Del Zanna 2011; Pili et al. 2014), that makes use of the extended conformal flatness approximation of Cordero-Carrión et al. (2009) and we study the angular momentum spectrum to estimate the resulting disk mass after collapse. We scrutinize our conclusions by simulating for a selected set of configurations the collapse directly with fully dynamical Numerical Relativity simulations. We summarize our numerical methods in Sec. 2, discuss the rotating equilibrium configurations in Sec. 3 and describe the dynamical collapse simulations in Sec. 4. Our results are summarized in Sec. 5. Comparisons between XNS and RNS results are provided in Appendix A.

2 NUMERICAL METHODS

2.1 Governing Equations

Our goal is to construct rigidly rotating neutron stars as pre-collapse initial conditions. We assume stationarity and axisymmetry and therefore can write the metric in quasi-

isotropic coordinates (t, r, θ, ϕ) (Gourgoulhon 2010) as

$$ds^2 = -N^2 dt^2 + A^2(dr^2 + r^2 d\theta^2) + r^2 B^2 \sin^2 \theta (d\phi - \omega dt)^2. \quad (2)$$

Here the cylindrical radius is defined as $R = Br \sin(\theta)$. The metric functions N, A, B, ω depend purely on r and θ , where N denotes the lapse and ω is the intrinsic angular momentum of a zero angular momentum observer (ZAMO).¹ The first integral (Gourgoulhon 2010) for a cold equation of state (EOS) in rigid rotation is

$$\ln h + \ln N - \ln W = \text{const}, \quad (3)$$

$$h = \frac{\epsilon + p}{\rho}, \quad (4)$$

$$W = (1 - U^2)^{-1/2}, \quad (5)$$

where h is the specific enthalpy, ϵ the total energy density, p the pressure, ρ the rest mass density, W the Lorentz factor, and U the magnitude of the fluid 3-velocity in the ZAMO reference frame. The fluid 3-velocity can be determined from the relations

$$U = R |U^\phi|, \quad \text{and} \quad U^\phi = \frac{\Omega - \omega}{N}, \quad (6)$$

where U^ϕ is the ϕ -component of the contravariant fluid 3-velocity and Ω is the star's angular velocity as seen by an observer at infinity, $\Omega \equiv \Omega(r, \theta)$.

Since the system we consider in this study can be considered to a very good approximation as being in cold β -equilibrium, we restrict ourselves to a barotropic EOS for which temperature effects can be neglected and all particle species are in equilibrium. Consequently, the EOS solely depends on the density, $p = p(\rho)$. A common choice is to impose a polytropic EOS of the type

$$p(\rho) = K \rho^\Gamma, \quad (7)$$

where K is called polytropic constant and Γ polytropic exponent. We combine multiple polytropes in different density regions to approximate more complicated and realistic EOSs (see e.g. Read et al. 2009). The obtained piecewise polytropic EOSs are still barotropic and hold as long as temperature effects can be neglected. Within this article we follow Read et al. (2009) and Margalit et al. (2015) in the construction of piecewise polytropic EOSs and assume a low density part ($\rho < \rho_0 = 10^{14.3} \text{ g cm}^{-3}$) approximating an SLy crust (Douchin & Haensel 2001; Read et al. 2009), see Tab. 1 and light blue line in Fig. 1. The high density part ($\rho > \rho_0 = 10^{14.3} \text{ g cm}^{-3}$) is a 2-pieces polytrope; see Tab. 1 and the dark blue line in Fig. 1. In this high density part, the first polytrope ($\rho_0 < \rho < \rho_1 = 10^{14.7} \text{ g cm}^{-3}$) is determined on one side by the SLy EOS that fixes the value of the pressure $p(\rho_0)$ and on the other side by the free parameter $p_1 \equiv p(\rho_1)$. The second polytrope ($\rho > \rho_1$) is determined by p_1 and by the polytropic exponent Γ_2 . Therefore, the whole EOS is fixed by only two parameters, p_1 and Γ_2 , cf. Tab. 1.

In the computation of the equilibrium configurations we neglect thermal effects, but we typically include them for

¹ ω is non-zero because of the frame dragging effect due to the rotation of the neutron star.

Table 1. Parameters of the piecewise polytropic EOS adopted in this paper. Density range ρ , polytropic exponent Γ , and polytropic constant K are reported in each column. The horizontal line separates the low-density SLy crust from the high-density core EOS. The quantities denoted with an asterisk ‘*’ depend on the choice of p_1 and Γ_2 . Beware that the dimensions of K depend on Γ .

ρ [g cm^{-3}]	Γ	K/c^2 [g cm^{-3}] $^{1-\Gamma}$
$< 2.44034 \times 10^7$	1.58425	6.80110×10^{-9}
$< 3.78358 \times 10^{11}$	1.28733	1.06186×10^{-6}
$< 2.62780 \times 10^{12}$	0.62223	$5.32697 \times 10^{+1}$
$< \rho_0 \equiv 1.99526 \times 10^{14}$	1.35692	3.99874×10^{-8}
$< \rho_1 \equiv 5.01187 \times 10^{14}$	*	*
$> \rho_1 \equiv 5.01187 \times 10^{14}$	Γ_2	*

the dynamical simulations, see Sec. 4, by adding a thermal pressure component to the barotropic pressure $p(\rho)$

$$p(\rho, \epsilon) = p(\rho) + \epsilon\rho(\Gamma_{\text{th}} - 1). \quad (8)$$

In accordance with previous work and following the discussion in Bauswein et al. (2010), where full tabulated EOSs are compared against the approximate description of Eq. (8), we employ $\Gamma_{\text{th}} = 1.75$. Additionally, we also perform a dynamical simulation without additional thermal component to allow for an assessment of systematic uncertainties.

2.2 Equilibrium configurations

Our investigation of the equilibrium configurations for different EOSs is based on the XNS code (Bucciantini & Del Zanna 2011; Pili et al. 2014), which determines the rotating stellar configuration in quasi-isotropic coordinates under the extended conformal flatness approximation (Cordero-Carrión et al. 2009). In the extended conformal flatness approximation, all elliptic equations that characterize the spacetime metric are hierarchically decoupled, which leads to a simplified metric with

$$A(r, \theta) \equiv B(r, \theta) \equiv \psi^2(r, \theta), \quad (9)$$

where ψ denotes the conformal factor. The approximation is justified since the metric functions A and B typically differ at most by about 0.1% (Gourgoulhon 2010).

For this study we have modified the publicly available version of XNS (Bucciantini & Del Zanna 2011; Pili et al. 2014) to the following workflow:

- (i) set the target stellar parameters central rest mass density, ρ_c , and angular speed seen by an observer at infinity, Ω .
- (ii) determine the initial configuration from the TOV solution (Tolman-Oppenheimer-Volkoff, namely the one that describe a spherical neutron star) with central density ρ_c , or if available, load a previously relaxed configuration from a sequence, obtained for example in the search for the Keplerian configuration.
- (iii) repeat until $\max_{r, \theta} |\rho_{\text{old}}(r, \theta) - \rho_{\text{new}}(r, \theta)| < 10^{-9} M_{\odot}^{-2}$ (in units $c = G = 1$):
 - (a) using the old metric and matter quantities, solve

the hierarchically decoupled equations of the extended conformal flatness approximation and update the metric fields.

- (b) update the matter fields solving the first integral, Eq. (3), with central density ρ_c and angular velocity Ω .

The main differences between our workflow and the original one are that we update the matter fields only through the first integral inversion avoiding conservative-to-primitive variable inversion. We directly set the central density in the first integral instead of using an external root-finding cycle, and we allow for an initial configuration other than the TOV one. Additional major technical modifications are the adoption of an inner (uniformly spaced) and an outer (increasingly spaced) radial grid, an angular grid defined on the Gauss-Legendre quadrature points, and the use of a true vacuum outside the neutron star instead of an artificial atmosphere.

The modified XNS version is ten times faster than RNS². In Appendix A we present a detailed convergence study and compare the results of our modified XNS version with the publicly available RNS code (Stergioulas & Friedman 1995). In particular, we find that XNS recovers the stellar properties within the precision of the extended conformal flatness approximation and yield practically identical results of RNS. For the exploration of the parameters space we employ XNS, while the initial configurations which we evolve dynamically with the BAM code are constructed with RNS, since the interface between RNS and BAM has been implemented and tested in detail in a previous work (Dietrich & Bernuzzi 2015).

2.3 Dynamical evolution

For the dynamical evolution we solve Einstein’s field equations in their 3+1 form recasted in the Z4c evolution system (Bernuzzi & Hilditch 2010; Hilditch et al. 2013). The gauge sector employs the 1+log and gamma-driver equations developed for black holes in the moving puncture approach (Bona et al. 1996; Alcubierre et al. 2003; van Meter et al. 2006; Campanelli et al. 2006; Baker et al. 2006). This particular gauge choice, often called ‘puncture gauge’, handles automatically the gravitational collapse of a neutron star to a black hole as discussed in Baiotti et al. (2007); Thierfelder et al. (2011a); Dietrich & Bernuzzi (2015) and is therefore particularly well-suited for our study.

The simulations are performed with the BAM code (Brügmann et al. 2008; Thierfelder et al. 2011b). BAM employs the method of lines approximating spatial derivatives of the metric variables by 4th order finite differences. Time integration is performed with an explicit 4th order Runge-Kutta scheme. The grid used in this work consists of a hierarchy of 7 cell-centered nested Cartesian boxes. Every box $l = 0, \dots, 6$ employs a constant grid spacing h_l and n points per direction. Boxes use a 2 : 1 refinement strategy, i.e., each coarser box employs a grid spacing $h_{l-1} = 2h_l$. For the time stepping of the mesh refinement, we employ the Berger-Oliger algorithm (Berger & Oliger 1984) extended

² On a 1.40GHz CPU (Intel(R) Core(TM) i3-2365M) and 4GB RAM laptop with -O2 optimization.

Table 2. Configurations employed for the dynamical evolutions. The columns refer to: configuration name, number of points in the Cartesian boxes, grid spacing in the refinement level covering the neutron star, atmosphere factor [see Eq. (10)], and flux limiter: WENOZ (Borges et al. 2008; Bernuzzi et al. 2012), linear total variation diminishing (LINTVD) (Shu & Osher 1989), 3rd order Essentially-Non-Oscillatory 3rd-order method (CENO3) (Liu & Osher 1998; Del Zanna et al. 2003). In addition to the listed setups, we also employ for one physical configuration the setup Res2^{WENOZ}_{atm19} but with zero thermal contribution, Eq. (8). This setup is labeled as Res2^{WENOZ}_{atm19cold}.

Name	n	$h_6 [M_\odot]$	f_{atm}	Limiter
Res1 ^{WENOZ} _{atm19}	120	0.1250	10^{-19}	WENOZ
Res2 ^{WENOZ} _{atm19}	180	0.0833	10^{-19}	WENOZ
Res3 ^{WENOZ} _{atm19}	240	0.0625	10^{-19}	WENOZ
Res4 ^{WENOZ} _{atm19}	360	0.0417	10^{-19}	WENOZ
Res2 ^{WENOZ} _{atm18}	180	0.0833	10^{-18}	WENOZ
Res2 ^{WENOZ} _{atm20}	180	0.0833	10^{-20}	WENOZ
Res2 ^{LINTVD} _{atm18}	180	0.0833	10^{-18}	LINTVD
Res2 ^{CENO3} _{atm20}	180	0.0833	10^{-20}	CENO3

by a refluxing step that enforces energy and momentum conservation across refinement boundaries (Berger & Colella 1989; East et al. 2012; Reisswig et al. 2013; Dietrich et al. 2015). The equations of GRHD are solved with a standard high-resolution-shock-capturing (HRSC) scheme based on primitive reconstruction and the Local-Lax-Friedrich central scheme for the numerical fluxes. The primitive reconstruction uses a fifth-order Weighted Essentially Non-Oscillatory (WENO) scheme (Borges et al. 2008; Bernuzzi et al. 2012), called WENOZ. Other limiters are used for comparison to assess the numerical uncertainties, see Tab. 2. The simulations presented in this article employ quadrant symmetry to reduce computational costs.

An important detail that is of particular interest for our study is the artificial atmosphere which is needed by GRHD simulations. As described in Thierfelder et al. (2011b) and Dietrich et al. (2015), we use a low-density static and barotropic atmosphere at a density level

$$\rho_{\text{atm}} = f_{\text{atm}} \cdot \max[\rho(t=0)]. \quad (10)$$

During the inversion from conservative to primitive variables we set a grid point to the atmosphere values if the density falls below the threshold

$$\rho_{\text{thr}} = f_{\text{thr}} \cdot \rho_{\text{atm}}. \quad (11)$$

Throughout this work we employ for the threshold $f_{\text{thr}} = 10^1$ and vary the value $f_{\text{atm}} = 10^{-18}, 10^{-19}, 10^{-20}$ to understand the effects of the artificial atmosphere on the debris disk mass. We also study numerical uncertainties by employing different grid resolutions. All employed combinations of resolutions, flux limiters, and atmosphere values are summarized in Tab. 2.

The initial conditions obtained (i.e., the equilibrium configurations) are ported onto the BAM grid by Lagrangian interpolation.

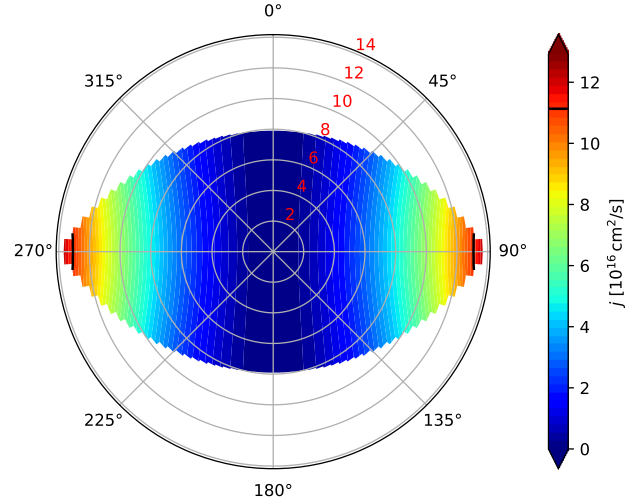


Figure 2. Specific angular momentum distribution for a neutron star in the Case A configuration (see text for details). The vertical direction correspond to the rotation axis and the red labels mark the radial coordinate (in km). The black solid contour corresponds to the angular momentum of a particle at the ISCO of a black hole with the same total mass and angular momentum of the neutron star. Only the matter on the outer side (dark red area) of the black contour can in principle escape black hole formation.

3 EQUILIBRIUM CONFIGURATIONS

In an axisymmetric dynamical system the spectrum of angular momentum, i.e., the integrated baryon rest mass of all fluid elements with a specific angular momentum, is strictly conserved in the absence of viscosity (Stark & Piran 1987). Even if some viscosity is present in either Nature or a numerical simulation, the (dynamical) collapse timescale are too short such that viscosity related effects have not time to grow. This suggests to use as a necessary condition for the formation of a debris disk that the specific angular momentum of a matter element at the stellar equator before the collapse is greater than the specific angular momentum of the innermost stable circular orbit (ISCO) of a Kerr BH with the same mass M and angular momentum J of the progenitor neutron star, see Fig. 2. This is also the criterion that has been applied in the study of Margalit et al. (2015). Since the specific angular momentum increases with the rotational frequency of the star, one expects that for a given EOS and central density ρ_c the collapse of a maximally rotating star (that rotates at the Keplerian frequency) will produce the largest debris disk mass. Furthermore, the configuration should be unstable to collapse to a BH.

In this section we state the stability and disk formation criteria, delineate our procedure to find the maximally rotating configurations, describe our results comparing them with Margalit et al. (2015), choose the configurations that we further analyze with dynamical simulations in the next section, and compute possible debris disk masses for a set of realistic EOSs constructed in Read et al. (2009).

3.1 Stability condition

If the star is non-rotating, the marginally stable configuration obeys (Sec. 10.11 of [Zeldovich & Novikov 1971](#))

$$\frac{dM}{d\rho_c} = 0. \quad (12)$$

Increasing the central density beyond this point the star becomes unstable and collapses to a BH. In the non-rotating case, this configuration also has the maximal gravitational mass.

For rotating stars the stability criterion has to be modified as follows ([Friedman et al. 1988](#))

$$\left. \frac{\partial M}{\partial \rho_c} \right|_J = 0, \quad (13)$$

where J is the total angular momentum. However, J is difficult to access during our computation with the XNS code since it uses ρ_c and Ω as input variables. One can circumvent this problem with a root finding cycle on J . Another possibility is to rewrite the stability condition (13) as

$$\left. \frac{\partial M}{\partial \rho_c} \right|_J = \left. \frac{\partial M}{\partial \rho_c} \right|_\Omega - \left. \frac{\partial J}{\partial \rho_c} \right|_\Omega \cdot \left. \frac{\partial M}{\partial \Omega} \right|_{\rho_c} \cdot \left(\left. \frac{\partial J}{\partial \Omega} \right|_{\rho_c} \right)^{-1}. \quad (14)$$

We have obtained Eq. (14) from

$$dM(\rho_c, J) = \left. \frac{\partial M}{\partial \rho_c} \right|_J d\rho_c + \left. \frac{\partial M}{\partial J} \right|_{\rho_c} dJ, \quad (15)$$

$$dM(\rho_c, \Omega) = \left. \frac{\partial M}{\partial \rho_c} \right|_\Omega d\rho_c + \left. \frac{\partial M}{\partial \Omega} \right|_{\rho_c} d\Omega, \quad (16)$$

$$dJ(\rho_c, \Omega) = \left. \frac{\partial J}{\partial \rho_c} \right|_\Omega d\rho_c + \left. \frac{\partial J}{\partial \Omega} \right|_{\rho_c} d\Omega. \quad (17)$$

One first equates Eqs. (15) and (16) (the total variation of the mass should be the same no matter which are the independent variables), then substitutes Eq. (17) and equates the terms that multiply $d\rho_c$. Eq. (14) is finally obtained using

$$\left. \frac{\partial M}{\partial J} \right|_{\rho_c} = \left. \frac{\partial M}{\partial \Omega} \right|_{\rho_c} \cdot \left. \frac{\partial \Omega}{\partial J} \right|_{\rho_c} = \left. \frac{\partial M}{\partial \Omega} \right|_{\rho_c} \cdot \left(\left. \frac{\partial J}{\partial \Omega} \right|_{\rho_c} \right)^{-1}, \quad (18)$$

where the equalities follow from the fact that, fixing ρ_c , the quantities M, J, Ω are functions of just one variable. Using Eq. (14) we can test the stability condition with only 3 configurations: those corresponding to (ρ_c, Ω) , $(\rho_c + d\rho_c, \Omega)$, and $(\rho_c, \Omega + d\Omega)$.³ Up to our knowledge this is the first time that Eq. (14) is discussed and used; we check it in the third panel of Fig. 3, where the solid red line refers to the value of $\partial M / \partial \rho_c|_J$ obtained through Eq. (14) and the dashed light blue line is obtained with a root-finding cycle on J . The two approaches agree within numerical uncertainties.

³ One can use Eqs. (14)–(18) also with the RNS code ([Stergioulas & Friedman Stergioulas & Friedman, 1995](#)), using $\epsilon_c = \epsilon(\rho_c)$ (energy density at the center) and $a \equiv r_{\text{surf}}(\theta = 0) / r_{\text{surf}}(\theta = \pi/2)$ (stellar quasi-isotropic radii ratio) as independent variables instead of ρ_c and Ω , respectively.

3.2 Disk formation condition

We use the specific angular momentum j of a fluid element (i.e., per baryon rest mass; e.g. Eq. (3.85) in [Gourgoulhon 2010](#))

$$j = hWR^2U^\phi. \quad (19)$$

The co-rotating ISCO specific angular momentum for a Kerr black hole with total gravitational mass M_{BH} and angular momentum J_{BH} is given by (Eqs. (2.12), (2.13), and (2.21) of [Bardeen et al. 1972](#))

$$j_{\text{ISCO}} = \sqrt{M_{\text{BH}}} \frac{r_{\text{ISCO}}^2 - 2\chi M_{\text{BH}}^{\frac{3}{2}} r_{\text{ISCO}}^{\frac{1}{2}} + \chi^2 M_{\text{BH}}^2}{d}, \quad (20)$$

with

$$\chi = \frac{J_{\text{BH}}}{M_{\text{BH}}^2}, \quad (21)$$

$$Z_1 = \sqrt[3]{1 - \chi^2} \left(\sqrt[3]{1 - \chi} + \sqrt[3]{\chi + 1} \right) + 1, \quad (22)$$

$$Z_2 = \sqrt{3\chi^2 + Z_1^2}, \quad (23)$$

$$d = r_{\text{ISCO}}^{\frac{3}{4}} \sqrt{r_{\text{ISCO}}^{\frac{3}{2}} - 3M_{\text{BH}} r_{\text{ISCO}}^{\frac{1}{2}} + 2\chi M_{\text{BH}}^{\frac{3}{2}}}, \quad (24)$$

$$r_{\text{ISCO}} = M_{\text{BH}} \left(3 + Z_2 - \sqrt{(3 - Z_1)(Z_1 + 2Z_2 + 3)} \right). \quad (25)$$

This allows to write the condition for disk formation as ([Shapiro 2004; Margalit et al. 2015](#))

$$j(r_{\text{surf}}, \pi/2) > j_{\text{ISCO}}(M_{\text{BH}} = M, J_{\text{BH}} = J), \quad (26)$$

where M and J are the neutron star gravitational mass and total angular momentum, and r_{surf} is the stellar radius. In Fig. 2 we plot the specific angular momentum distribution in a neutron star. The black line corresponds to the ISCO angular momentum and divides the material which will collapse into the forming black hole and that will form a debris disk. We remark that, to be fully consistent, we should have taken a black hole with a total mass and angular momentum equal to that of the pre-collapse neutron star *without* the contribution from the debris disk. This could be accomplished within an iterative procedure ([Shapiro 2004](#)). However, such a procedure is not well defined since the local energy is not well defined in General Relativity and hence in a neutron star. In any case we have checked that the results obtained with the iterative procedure are indistinguishable from those obtained without it because the debris disk has very little mass and angular momentum (see discussion below).

3.3 Parameter space exploration

Following the above discussion we estimate, for each choice of the EOS (specified by parameters p_1 and Γ_2), the baryonic mass of the disk that can be generated from the collapse of the maximally rotating (Keplerian) configuration. We remark that in general the marginally stable Keplerian configuration, which is the stable configuration with greater angular velocity, *is not* the configuration with maximal gravitational mass at the Kepler frequency (see e.g. Fig. 2 in [Stergioulas & Friedman 1995](#) or Fig. 3 of this paper).

The code settings adopted in the parameter space exploration are the same of the “baseline” configuration described in Appendix A, apart for the radius of the inner grid which is set to 20 (in code units, see Appendix A for

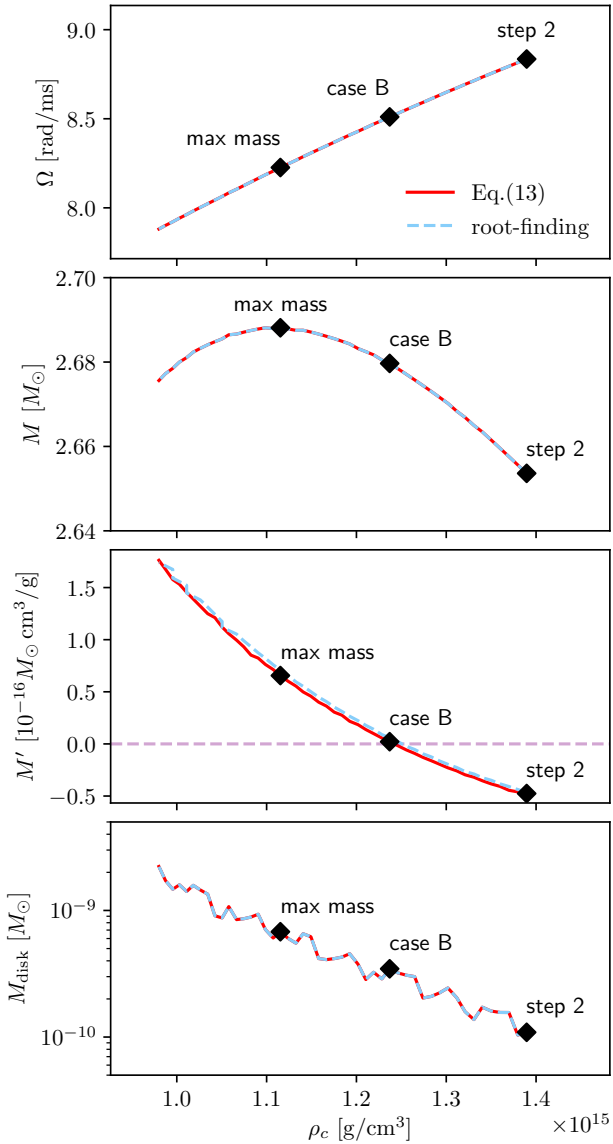


Figure 3. Initial configuration search (extended to lower densities on the Keplerian line) for the piecewise polytropic EOS corresponding to Case B (see Tab. 3). The configurations discussed in the text are marked. From top to bottom we show the angular frequency Ω , the gravitational mass M , the partial derivative at constant J : $M' \equiv \partial M / \partial \rho_c|_J$, and the baryonic mass of the disk estimated from the equilibrium configuration M_{disk} [i.e., the baryon mass of the material that fulfill Eq. (26)], all plotted against the central density ρ_c . The solid red lines are obtained using Eq. (14) and the dashed light blue lines are obtained with a root-finding cycle on J . The results of the two approaches differ only in M' , in which case are consistent within the numerical uncertainties.

details). Our procedure to find the interesting stellar models, for each choice of the EOS parameters p_1 and Γ_2 , is:

- (1) start from the maximal TOV (spherical) mass configuration, with $\Omega = 0$ and central density ρ_c .
- (2) keep ρ_c fixed and increase Ω until the Keplerian (i.e., maximally rotating) configuration is reached. We will

refer to this configuration as “step 2”⁴. The Keplerian angular speed Ω_K is determined by evaluating the co-rotating case of Eq. (4.93) of Gourgoulhon (2010) at the equator,

$$\Omega_K = \omega + \frac{\omega' R}{2R'} + \sqrt{\frac{N' N}{R' R} + \left(\frac{\omega' R}{2R'}\right)^2}, \quad (27)$$

where all quantities are evaluated at the equator and primes denote derivatives along the radial direction r .

(3) repeat:

- (a) compute $\partial M / \partial \rho_c|_J$ [Eq. (14)] varying ρ_c and Ω .
- (b) if $\partial M / \partial \rho_c|_J \geq 0$, the configuration is maximally rotating and at the verge of collapse (i.e., it is the marginally stable Keplerian configuration).
- (c) if the mass is lower than that of the previous configuration, the previous is the maximal mass one.
- (d) once the maximal mass configuration and the marginally stable Keplerian configuration are found, exit the cycle.
- (e) reduce Ω by $d\Omega = 10^{-4} M_\odot^{-1}$ ($c = G = 1$ units).
- (f) reduce ρ_c until you reach the Keplerian configuration.

In general, the step 2 and the maximal mass configurations can be stable or unstable (Stergioulas & Friedman 1995). As an example, in Fig. 3 we report the search for a case in which the maximal mass configuration is stable and the step 2 configuration is unstable, which is the most common case in our analysis.

We estimate the mass of the debris disk from a given equilibrium configuration integrating the baryon mass in the neutron star that fulfills the condition $j(r, \theta) > j_{\text{ISCO}}$ (lower plot of Fig. 4). This estimated disk mass increases as we step to lower central densities along the Keplerian curve (see lower plot in Fig. 3). However, these lower density configurations would not give rise to a debris disk because they are stable.

We have explored the same EOS parameter space as Margalit et al. (2015), namely $p_1 \in [10^{33.8}; 10^{35.2}]$ dyne cm^{-3} and $\Gamma_2 \in [1.1; 4]$, our results are shown in Fig. 4. Most of the EOS parameter choices result in disk formation; moreover the general trend is that the greater the maximal mass (stiffer EOSs, i.e., greater p_1 and Γ_2), the smaller the disk mass of the marginally stable Keplerian configuration.

We select a few configurations that we also study with fully dynamic Numerical Relativity simulations (Cases A, \tilde{A} , B, and C, see marks in Fig. 4). These configurations are reported in Tab. 3. The rationale behind our choices is the following:

A marginally stable Keplerian configuration with the greatest disk mass compatible with the request to have a maximal TOV mass greater than $1.5M_\odot$, see upper plot in Fig. 4. The corresponding value of $\Gamma_2 = 1.3$ is substantially smaller than what is considered realistic (≥ 2.5 ; e.g. Fig. 5 in Rosswog & Davies 2002).

⁴ For most of the EOS parameter space considered in this paper, the step 2 configuration is unstable ($\partial M / \partial \rho_c|_J < 0$) and has a central density greater than that of the maximal mass configuration (see Fig. 3). When this does not hold, for very low p_1 and Γ_2 , we have re-started the search from a greater central density.

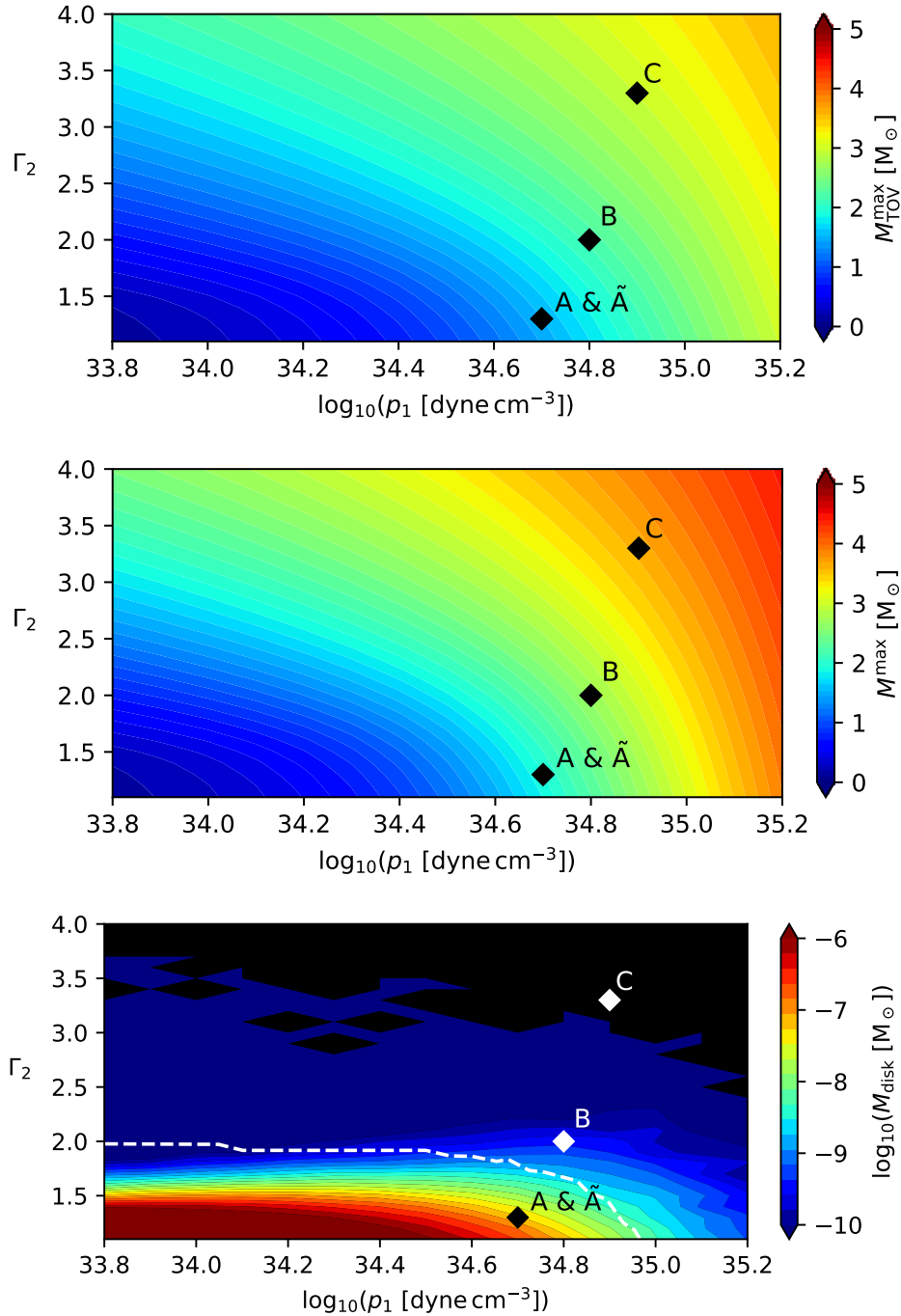


Figure 4. Stellar properties dependence on the EOS parameters p_1 and Γ_2 . From top to bottom: maximal TOV gravitational mass, maximal gravitational mass (at the Keplerian frequency), and estimated disk baryon mass of the marginally stable Keplerian configuration. The black area in the lower plot represents the parameter space for which no disk formation is possible ($M_{\text{disk}} = 0$). We mark with diamonds the configurations that we have further studied with dynamical simulations. The white dashed line denotes the disk/no-disk separation curve previously found by [Margalit et al. \(2015\)](#).

\tilde{A} maximal mass configuration equivalent to another Case studied with a dynamical simulation that results in a collapse to test our prediction on the stability of the maximal mass configuration (we picked a stable case).

B marginally stable Keplerian configuration with the maximal TOV mass equal to $2M_{\odot}$ and $\Gamma_2 = 2$. This choice of the high density polytropic exponent is still smaller than

current predictions but it is a common choice in many numerical applications.

C marginally stable Keplerian configuration with no predicted disk and a maximal TOV mass smaller than $3M_{\odot}$.

Table 3. Properties of the configurations marked in Fig. 4 and described in Sec. 3.3. The columns contain, in order: the configuration name (“Case”); the EOS parameters (p_1 in dyne cm^{-3} and Γ_2); the configuration parameters (central density ρ_c , angular speed seen by an observer at infinity Ω , axes ratio a , gravitational mass M); and the disk baryon mass (both determined from the equilibrium configuration $M_{\text{disk}}^{\text{eq}}$ and from the dynamical simulation about 8 ms after its beginning $M_{\text{disk}}^{\text{dyn}}$). Note that Case \tilde{A} does not collapse, as expected.

Case	$\log_{10}(p_1)$	Γ_2	$\rho_c [10^{15} \text{ g cm}^{-3}]$	$\Omega [\text{rad/ms}]$	a	$M [M_\odot]$	$M_{\text{disk}}^{\text{eq}} [M_\odot]$	$M_{\text{disk}}^{\text{dyn}} [M_\odot]$
A	34.7	1.3	1.212	7.016	0.5567	1.924	7×10^{-8}	$\lesssim 10^{-7}$
\tilde{A}	34.7	1.3	1.033	6.834	0.5524	1.933	-	-
B	34.8	2.0	1.238	8.511	0.5599	2.679	3×10^{-10}	$\lesssim 10^{-7}$
C	34.9	3.3	0.9634	9.573	0.5630	3.614	4×10^{-13}	$\lesssim 10^{-8}$

3.4 Comparison with Margalit et al. (2015)

While in good qualitative agreement, our results differ quantitatively from those of Margalit et al. (2015). In fact, we find that disk formation is possible also for $\Gamma_2 \gtrsim 2$ and $\log_{10}(p_1/\text{dyne cm}^{-2}) \gtrsim 34.9$, cf. lower panel of Fig. 4. None of the cases considered in our study, however, is a candidate for producing an sGRB, because the disk mass is too small, cf. Eq. (1).

In principle, the main difference in the employed methods between our work and Margalit et al. (2015) are:

- Margalit et al. (2015) uses the RNS code, while we use XNS. As we show in Appendix A, the configurations found by both codes are in good agreement.
- Margalit et al. (2015) searches for the maximal mass configuration instead of the marginally stable configuration. As argued in Sec. 3.3 and in Stergioulas & Friedman (1995), the maximal mass configuration is not necessarily unstable, because the stability condition should be checked at constant J , and in any case it is not on the verge of instability. However, we checked that the maximal mass configuration generates a disk similar to that of the marginally stable Keplerian configuration.

We note that the step 2 configuration actually reproduces Fig. 2 of Margalit et al. (2015). However, this configuration is unstable for most of the choices of the EOS parameters (apart for very small p_1 and Γ_2) and was not considered in our analysis.

3.5 Fit to realistic EOSs of Read et al. (2009)

In addition to the general consideration of neutron stars described by a 2-piece polytropic core, we have applied the outlined procedure to some more realistic multi-piecewise polytropic EOSs. Those fits have been constructed in Read et al. (2009) and model EOSs describing full tabulated EOSs for different nuclear physical models. The results for these EOSs are given in Tab. 4. We have chosen this subset of EOSs since it is in agreement with current observations: (i) maximum supported masses are above $2.0M_\odot$ (Antoniadis et al. 2013); (ii) maximum supported masses are below $\sim 2.3M_\odot$ (Rezzolla et al. 2017; Shibata et al. 2017; Ruiz et al. 2017; Margalit & Metzger 2017); and (iii) the compactness and tidal deformability are in agreement with the measurements obtained from GW170817 (Abbott et al. 2017a; Abbott et al. 2018). The results for realistic EOSs confirm the conclusions for the EOS parameter search made in this section, namely that even if a debris disk

Table 4. Disk formation for some realistic EOSs (see text for details), whose piecewise polytropic fit is given in Read et al. (2009) (with an SLy crust at low densities). We report the EOS name (1st column), the gravitational mass of the maximal mass configuration (2nd column), the angular velocity and disk baryonic mass estimated from the equilibrium model of the marginally stable Keplerian configuration (3rd and 4th columns respectively). We remark that the angular velocity of the marginally stable Keplerian configuration is also the maximal one for stable configurations, see Fig. 3.

EOS	$M^{\text{max}} [M_\odot]$	$\Omega [\text{rad/ms}]$	$M_{\text{disk}}^{\text{eq}} [M_\odot]$
SLy	2.415	11.50	5×10^{-13}
APR4	2.594	12.32	2×10^{-12}
WFF1	2.534	13.54	8×10^{-13}
WFF2	2.604	12.67	1×10^{-13}
ENG	2.656	11.52	3×10^{-12}
ALF2	2.399	9.187	2×10^{-10}

can form, its mass is too small to generate an energetic GRB.

An important point to stress here is that we are discussing the mass and the extractable GRB energy of a debris disk formed by material of the pre-collapse neutron star. This means that we are not addressing the possibility that the GRB is caused by a pre-existing debris disk (Michel & Dessler 1981), for example due to fallback from the original supernova event. These disks may even be more massive than the disks we predict in our analysis (e.g., Wang et al. 2006 found observational evidence of a fallback disk of $\sim 10^{-5}M_\odot$, see also Wang 2014 for a recent review).

4 DYNAMICAL EVOLUTIONS

In the following we study the configurations marked in Fig. 4 and described in Tab. 3 and Sec. 3.3 to determine whether dynamical effects can facilitate the debris disk formation.

4.1 Cases A and \tilde{A}

Cases A and \tilde{A} employ an EOS with $\log(p_1) = 34.7$ and $\Gamma_2 = 1.3$, see Tab. 3. The Case A (marginally stable Keplerian configuration) is characterized by a central density of $\rho_c = 1.212 \times 10^{15} \text{ g/cm}^3$ and an angular speed of $\Omega = 7.016 \text{ rad/ms}$. The Case \tilde{A} (maximal mass configuration) has a central density $\sim 15\%$ lower than Case A and

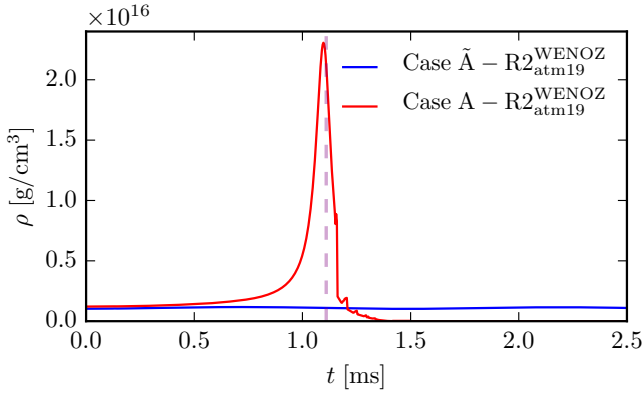


Figure 5. Maximum density for the maximal mass configuration (Case \tilde{A} , blue line) and marginally stable Keplerian configuration (Case A, red line). We mark the formation of the apparent horizon for Case A with a vertical purple dashed line.

an angular speed of $\Omega = 6.834$ rad/ms. Within our simulations we trigger the gravitational collapse by introducing a small artificial pressure perturbation. This is a common approach for the study of gravitational collapse. Generally, large perturbations lead to a faster collapse which reduces the computational cost of the individual simulations, but on the other hand it might affect the dynamical evolution. We employ a small perturbation of 0.05% to reduce nonphysical effects⁵, reminding the reader that the introduced pressure perturbation leads to Hamiltonian constraint violations at $t = 0$. Previous studies have used larger perturbations, see e.g. [Giacomazzo & Perna \(2012\)](#) where a 0.1% perturbation, [Dietrich & Bernuzzi \(2015\)](#) where a 0.5% perturbation, and [Baiotti et al. \(2005, 2007\)](#); [Reisswig et al. \(2013\)](#) where a 2% perturbation were applied.

Comparison of maximal mass and marginally stable Keplerian configurations. Before discussing the gravitational collapse in detail, we compare the simulations of the maximal mass and the marginally stable Keplerian configurations. Figure 5 shows the maximum density evolution for both cases, where the maximal mass configuration is shown in blue (Case \tilde{A}) and the marginally stable Keplerian configuration in red (Case A). We find that, as outlined in our previous discussion (Sec. 3.1), the maximal mass configuration is stable and does not undergo gravitational collapse while the marginally stable Keplerian configuration is characterized by a rapid increase of the central density until a BH forms at ~ 1 ms after the begin of the simulation. The vertical dashed line in Fig. 5 denotes the horizon formation. For the maximal mass model we find small density oscillations introduced by the pressure perturbation (not visible at the density scale of Fig. 5). Whereas these oscillations are too small to cause a gravitational collapse, imposing a larger pressure perturbation would have led to BH formation also for the maximal mass configuration.

⁵ We also performed a subset of simulations with different pressure perturbations and find consistent results.

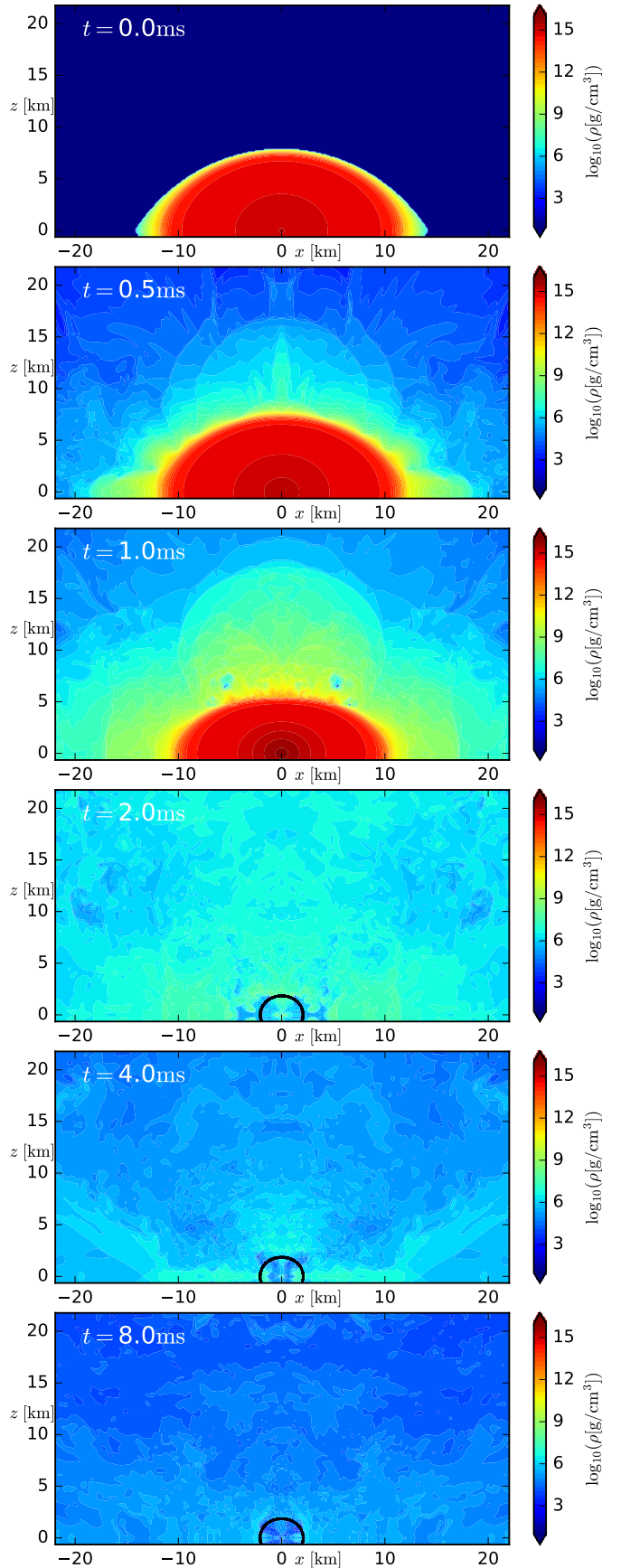


Figure 6. Snapshots of the density profile in the x-z-plane at $t = 0, 0.5, 1.0, 2.0, 4.0, 8.0$ ms for the Case A. The snapshot times are marked in Fig. 7 with black diamonds. The black solid line marks the BH horizon.

Collapse morphology. In the following we discuss the dynamics during the gravitational collapse of the marginally stable Keplerian model. For this purpose we show for different instants of times the density within the x-z-plane (corresponding to a slice with constant ϕ in the equilibrium case) in Fig. 6. The shown time snapshots are marked in Fig. 7, where we report the disk mass estimated as average of the two highest resolutions (the shaded region shows the difference between these simulations). The top panel of Fig. 6 shows the initial equilibrium configuration at $t = 0$ ms. The stellar shape is characterized by its oblate form due to the large intrinsic rotation.

At $t = 0.5$ ms (second panel of Fig. 6) the stellar surface is less sharp compared to the initial configuration. This is typically observed in all Numerical Relativity simulations of neutron star spacetimes using grid-based codes, see e.g. Guercilena et al. (2017) for further discussions. It is introduced by the fact that the numerical scheme is unable to resolve the sharp, step-like surface of the star. This effect becomes even more pronounced due to artificial shock heating at the stellar surface. While an increased resolution and less dissipative schemes for the numerical fluxes reduce the effect, there are currently no full 3D Numerical Relativity simulations of dynamical spacetimes which retain the exact shape of the surface. We suggest that due to this effect Numerical Relativity simulations are likely to overestimate the material surrounding the NS.

At $t = 1.0$ ms (third panel of Fig. 6) the star has further contracted and the central density has increased. Most notably some low density material leaves the star with high velocity along the z-axis. This matter becomes unbound and is ejected from the system. We mark material as unbound/ejected once the geodesic criterion is fulfilled, i.e., when the time-component of the four-velocity is $u_t < -1$ and when the radial component of the velocity is positive. The ejection of material is caused by shocks at the stellar surface. Since those shocks might be associated to the artificial atmosphere employed in the dynamical evolution, we assess the error of the numerical method by simulating configurations with different resolutions and atmosphere values, as well as flux limiting schemes, see Fig. 9 and the discussion below.

At $t = 2$ ms (forth panel of Fig. 6), the star has collapsed to a BH; we mark the apparent horizon with a black solid line. The density dropped several orders of magnitude and reaches now maximum values of $\rho \sim 10^7 \text{g/cm}^3$. At this time the bound mass (namely, the debris disk mass) has decreased to $M_{\text{disk}} \approx 10^{-6} M_{\odot}$.

At $t = 4$ ms (fifth panel of Fig. 6), the density decreases further to $\rho \sim 10^6 \text{g/cm}^3$ and finally at $t = 8$ ms (last panel) the density surrounding the central BH has dropped to $\rho \lesssim 10^5 \text{g/cm}^3$. The final disk mass at this time has settled at about $\sim 10^{-7} M_{\odot}$.

4.2 Case B

For Case B we employ an EOS characterized by $\log(p_1) = 34.8$ and $\Gamma_2 = 2.0$. The marginally stable Keplerian configuration has a central density of $\rho_c = 1.238 \times 10^{15} \text{g/cm}^3$ and an angular velocity of $\Omega = 8.511 \text{rad/ms}$. Since the collapse dynamics follows the same qualitative steps outlines for Case A in Fig. 6, we restrict our considerations to quantitative

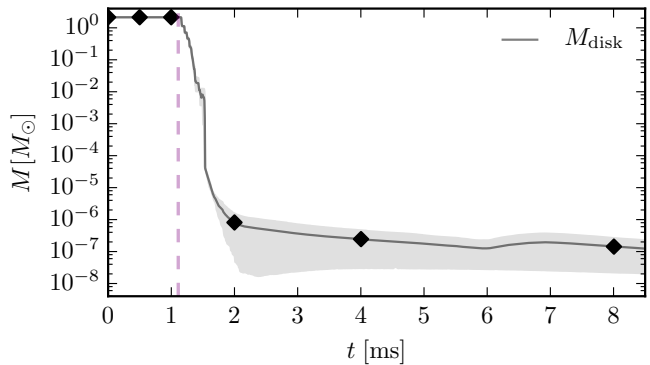


Figure 7. Evolution of the bound (disk) mass for Case A. Black diamonds refer to the times shown in Fig. 6 and the vertical dashed purple line to the formation time of the apparent horizon. The shaded region shows the difference between the two higher resolution simulations.

statements. The debris disk mass is slightly smaller than for Case A, as expected from our findings for the equilibrium configuration, but overall also of the order of $\sim 10^{-7} M_{\odot}$. Similarly to Case A we obtain an ejecta mass of the order of $10^{-4} M_{\odot}$; see discussion below for more details.

4.3 Case C

Case C employs an EOS determined by $\log(p_1) = 34.9$ and $\Gamma_2 = 3.3$. The marginally stable Keplerian configuration has a central density of $\rho_c = 9.634 \times 10^{14} \text{g/cm}^3$ and an angular speed of $\Omega = 9.573 \text{rad/ms}$. We find for this setup that the mass of the disk (bound material) falls below $10^{-10} M_{\odot}$ about 2 ms after BH formation. The increase of bound mass after this time might be caused either by material which is initially marked as unbound and later falls back onto the remnant⁶ or simply by inaccuracies of the numerical scheme. However, overall Case C produces the smallest amount of bound material as expected from the equilibrium configuration analysis.

4.4 Accessing the numerical uncertainty

Fig. 9 gives an overview of the bound (disk) mass and the unbound (ejecta) mass for all simulations of Case A.

Artificial atmosphere. Let us start by considering the imprint of the artificial atmosphere, cf. green lines in top and bottom panels. Although the artificial atmosphere threshold has been varied by a factor of 100, we find that the disk and ejecta masses are almost unchanged. Therefore, although the artificial atmosphere introduces errors, the previous conclusions remain valid.

⁶ It is possible that material which is first marked as unbound falls back onto the remnant, since the geodesic criterion used to characterize fluid elements assumes that fluid elements follow a geodesic motion, which is only approximately correct for a dynamical spacetimes as the one considered in this article.

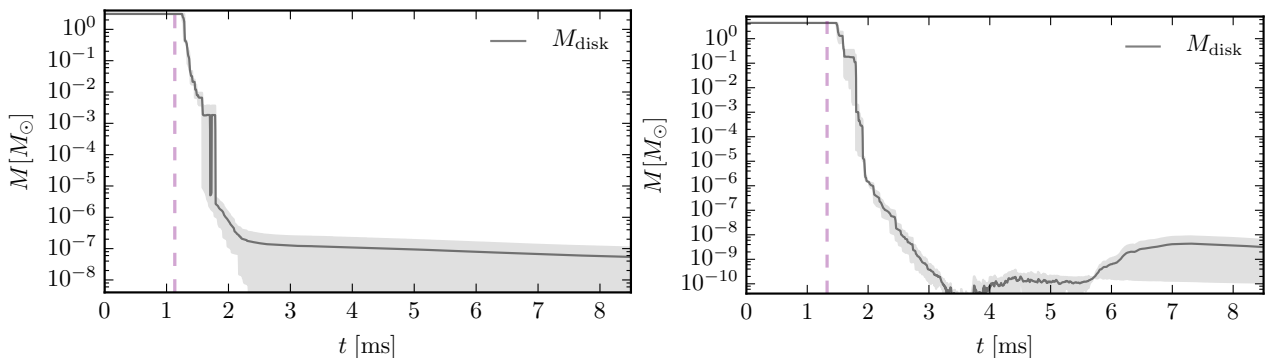


Figure 8. Evolution of the bound (disk) mass for Case B (left panel) and Case C (right panel). The vertical dashed, purple lines mark the formation time of an apparent horizon and the shaded region represents the differences between the two higher resolution simulations.

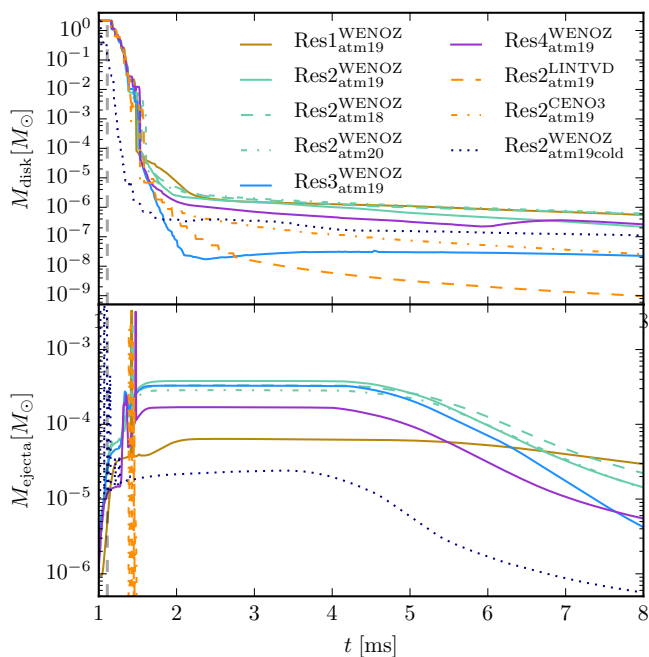


Figure 9. Evolution of the bound (top panel) and the unbound (lower panel) baryonic mass for different resolutions, atmosphere settings, and numerical flux limiters. The vertical dashed line refers to the apparent horizon formation for setup $\text{Res4}_{\text{atm19}}^{\text{WENOZ}}$. Note that the main reason for the decrease in the ejecta mass after about ~ 5 ms (see Fig. 7) is the material which leaves the numerical domain covered by our simulation.

Resolution. We continue the discussion by focusing on the simulations with different resolutions. We have varied the resolution by a factor of three, which generally is a very large range for full Numerical Relativity simulations where computational costs scale with the fourth power of the number of grid points. We do find that the results are not monotonically converging with increasing resolution. This behavior is unfortunately often seen in full 3D Numerical Relativity simulations estimating disk and ejecta masses, see e.g. [Hotokezaka et al. \(2013\)](#); [Dietrich & Ujevic \(2017\)](#); [Fujibayashi et al. \(2017\)](#). However, although precise statement about the bound/unbound mass can not be made, the fact that the mass estimates change only about one order of magnitude

for the large range of resolutions employed leads to the conclusion that the order of magnitude estimates necessary for our study are indeed valid.

Numerical flux limiter. We also discuss the imprint of the flux limiter used in the GRHD scheme. For this purpose we employ 3 different flux reconstruction schemes: LINTVD ([Shu & Osher 1989](#)), CENO3 ([Liu & Osher 1998](#); [Del Zanna et al. 2003](#)), and WENOZ ([Borges et al. 2008](#); [Bernuzzi et al. 2012](#)). As expected we find that less sophisticated, lower order schemes as LINTVD and CENO3 predict smaller bound and unbound masses. In particular the ejecta mass drops to zero for these two schemes. This analysis shows that high order flux limiters as WENOZ seem to be required for a proper modeling of the system. Although we can not exclude that with even more improved HRSC methods larger disk masses might be observed, we do expect that the results are robust and allow order of magnitude estimates. This statement is based on investigations of binary systems that show that the WENOZ reconstruction scheme is among the state-of-the-art methods and allows accurate and reliable simulations of neutron star spacetimes, see e.g. [Bernuzzi et al. \(2012\)](#); [Bernuzzi & Dietrich \(2016\)](#).

Thermal effects. Finally, we consider the imprint of the thermal effects added through Eq. (8). For this purpose we compare the setups $\text{Res2}_{\text{atm19}}^{\text{WENOZ}}$ and $\text{Res2}_{\text{atm19cold}}^{\text{WENOZ}}$. We find that while the disk mass is compatible with simulations including thermal effects, the ejecta mass is reduced. This supports our suggestion that most of the ejecta is caused by shock heating. Consequently, although we found that the ejecta mass is not affected by resolution and is robustly around $10^{-4} M_{\odot}$, we can not rule out that the shock heating is artificially caused by the numerical scheme and not caused by a physical mechanism.

5 SUMMARY

We have performed a detailed analysis of the conditions under which a supramassive neutron star can collapse to a Kerr black hole surrounded by an accretion disk. Our approach has been two-fold: we first analyzed the angular momentum spectrum of the collapsing configurations and subsequently performed dynamical 3D collapse simulations to

confirm our findings. We constructed rigidly rotating initial neutron stars using the XNS code (Bucciantini & Del Zanna 2011; Pili et al. 2014). These initial configurations were analyzed for the mass that has enough angular momentum to remain outside of the ISCO of the forming black hole. A similar study has recently been performed by Margalit et al. (2015) who used the RNS code (Stergioulas & Friedman 1995). We argue here that, contrary to what has been done in their work, the configuration that can collapse to a BH is not the maximal mass configuration, but instead the marginally stable Keplerian configuration, for which $\partial M/\partial \rho_c|_J = 0$. Moreover, we find that a disk can form for a larger volume of the parameter space, albeit its mass is very small. Despite these small differences we confirm their main result that it is very difficult to form a massive disk from a collapsing neutron star and all the cases that were investigated fall short by orders of magnitude to produce an energetic sGRB. These conclusions were subsequently confirmed by fully dynamical Numerical Relativity simulations performed with the BAM code (Brügmann et al. 2008; Thierfelder et al. 2011b).

In this work, we have assumed uniform rotation and a cold EOS for the initial configurations of the collapsing stars. The uniform rotation is justified by the sGRB models that motivate this study. If the supramassive NS is formed by accretion from a non-degenerate companion star (MacFadyen et al. 2005), there is no reason to expect differential rotation. At the moment of collapse, however, the NS —while being essentially cold throughout the bulk of the high-density matter— may be engulfed by a high-temperature envelope, which is not modelled in this work.

If, in contrast, the supramassive neutron star is formed as a result of a neutron star merger, as invoked by “time reversal models” (Ciolfi & Siegel 2015; Rezzolla & Kumar 2015), it is expected to be both hot ($\gtrsim 10$ MeV) and differentially rotating, at least initially. Such differentially rotating, “hypermassive” neutron stars can support a substantially larger mass than rigidly rotating ones, but magnetic braking and viscosity will drive the stars to collapse on a short time scale even if the initial seed magnetic field is low and viscosity is small (Shapiro 2000). Therefore, neutron stars that remain stable for long enough to explain the long term X-ray emission ($\sim 10^4$ s), have likely dissipated their differential rotation and have cooled to temperatures where thermal effects in the high-density matter are small, since the Kelvin-Helmholtz neutrino cooling time is of the order of only seconds. Therefore, we consider also in this case our assumption of essentially cold EOS and rigid rotation as plausible.

For the equations of state expected in neutron stars ($\Gamma > 2$), the resulting disk masses after the collapse are orders of magnitude lower ($\lesssim 10^{-7} M_\odot$) than what is needed for a typical sGRB. Therefore, we interpret this result as disfavoring those sGRB models that require the collapse of a supramassive NS into a BH plus disk configuration.

ACKNOWLEDGEMENTS

T.D. acknowledges support by the European Union’s Horizon 2020 research and innovation program under grant agreement No 749145, BNSmergers. Computations were performed on the supercomputer SuperMUC at the LRZ (Mu-

nich) under the project number pr48pu and on the compute cluster Minerva of the Max-Planck Institute for Gravitational Physics.

S.R. has been supported by the Swedish Research Council (VR) under grant number 2016-03657_3, by the Swedish National Space Board under grant number Dnr. 107/16 and by the research environment grant Gravitational Radiation and Electromagnetic Astrophysical Transients (GREAT)” funded by the Swedish Research council (VR) under Dnr. 2016-06012.

We acknowledge support from the COST Action PHAROS (CA16214).

We are grateful to A. Pili, N. Bucciantini, and L. Del Zanna for making the XNS code public available and for useful discussion.

REFERENCES

- Abbott B. P., et al., 2017a, *Physical Review Letters*, **119**, 161101
 Abbott B. P., et al., 2017b, *Nature*, **551**, 85
 Abbott B. P., et al., 2017c, *ApJL*, **848**, L12
 Abbott B. P., et al., 2018, preprint ([arXiv:1805.11579](https://arxiv.org/abs/1805.11579))
 Alcubierre M., Brügmann B., Diener P., Koppitz M., Pollney D., et al., 2003, *Phys.Rev.*, **D67**, 084023
 Antoniadis J., Freire P. C., Wex N., Tauris T. M., Lynch R. S., et al., 2013, *Science*, **340**, 6131
 Baiotti L., Hawke I., Montero P. J., Loffler F., Rezzolla L., et al., 2005, *Phys.Rev.*, **D71**, 024035
 Baiotti L., Hawke I., Rezzolla L., 2007, *Class. Quant. Grav.*, **24**, S187
 Baker J. G., Centrella J., Choi D.-I., Koppitz M., van Meter J., 2006, *Phys. Rev. Lett.*, **96**, 111102
 Bardeen J. M., Press W. H., Teukolsky S. A., 1972, *ApJ*, **178**, 347
 Barthelmy S. D., et al., 2005, *Nature*, **438**, 994
 Bauswein A., Janka H.-T., Oechslin R., 2010, *Phys.Rev.*, **D82**, 084043
 Berger E., 2014, *Ann.Rev.Astron.Astrophys.*, **52**, 43
 Berger M. J., Colella P., 1989, *Journal of Computational Physics*, **82**, 64
 Berger M. J., Oliger J., 1984, *J.Comput.Phys.*, **53**, 484
 Bernuzzi S., Dietrich T., 2016, *Phys. Rev.*, **D94**, 064062
 Bernuzzi S., Hilditch D., 2010, *Phys. Rev.*, **D81**, 084003
 Bernuzzi S., Nagar A., Thierfelder M., Brügmann B., 2012, *Phys.Rev.*, **D86**, 044030
 Bona C., Massó J., Stela J., Seidel E., 1996, in Jantzen R. T., Keiser G. M., Ruffini R., eds, *The Seventh Marcel Grossmann Meeting: On Recent Developments in Theoretical and Experimental General Relativity, Gravitation, and Relativistic Field Theories*. World Scientific, Singapore
 Borges R., Carmona M., Costa B., Don W. S., 2008, *Journal of Computational Physics*, **227**, 3191
 Brügmann B., Gonzalez J. A., Hannam M., Husa S., Sperhake U., et al., 2008, *Phys.Rev.*, **D77**, 024027
 Bucciantini N., Del Zanna L., 2011, *A&A*, **528**, A101
 Campanelli M., Lousto C. O., Marronetti P., Zlochower Y., 2006, *Phys. Rev. Lett.*, **96**, 111101
 Ciolfi R., Siegel D. M., 2015, *ApJ*, **798**, L36
 Cordero-Carrión I., Cerdá-Durán P., Dimmelmeier H., Jaramillo J. L., Novak J., Gourgoulhon E., 2009, *Phys. Rev. D*, **79**, 024017
 Cowperthwaite P. S., Berger E., Villar V. A., Metzger B. D., 2017, *ApJL*, **848**, L17
 Del Zanna L., Bucciantini N., Londrillo P., 2003, *Astron. Astrophys.*, **400**, 397
 Dietrich T., Bernuzzi S., 2015, *Phys.Rev.*, **D91**, 044039

Dietrich T., Ujevic M., 2017, *Class. Quant. Grav.*, 34, 105014
 Dietrich T., Bernuzzi S., Ujevic M., Brüggmann B., 2015, *Phys. Rev.*, D91, 124041
 Douchin F., Haensel P., 2001, *Astron. Astrophys.*, 380, 151
 East W. E., Pretorius F., Stephens B. C., 2012, *Phys.Rev.*, D85, 124010
 Eichler D., Livio M., Piran T., Schramm D. N., 1989, *Nature*, 340, 126
 Fong W., Berger E., Margutti R., Zauderer B. A., 2015, *ApJ*, 815, 102
 Freiburghaus C., Rosswog S., Thielemann F.-K., 1999, *ApJ*, 525, L121
 Friedman J. L., Ipser J. R., Sorkin R. D., 1988, *ApJ*, 325, 722
 Fujibayashi S., Kiuchi K., Nishimura N., Sekiguchi Y., Shibata M., 2017, preprint ([arXiv:1711.02093](https://arxiv.org/abs/1711.02093))
 Giacomazzo B., Perna R., 2012, *Astrophys.J.*, 758, L8
 Gompertz B. P., O'Brien P. T., Wynn G. A., 2014, *MNRAS*, 438, 240
 Gourgoulhon E., 2010, preprint, ([arXiv:1003.5015v2](https://arxiv.org/abs/1003.5015v2))
 Guercilena F., Radice D., Rezzolla L., 2017, *Comput. Astrophys. Cosmol.*, 4, 3
 Hilditch D., Bernuzzi S., Thierfelder M., Cao Z., Tichy W., et al., 2013, *Phys. Rev.*, D88, 084057
 Hotokezaka K., Kiuchi K., Kyutoku K., Okawa H., Sekiguchi Y.-i., et al., 2013, *Phys.Rev.*, D87, 024001
 Kasen D., Metzger B., Barnes J., Quataert E., Ramirez-Ruiz E., 2017, *Nature*
 Kasliwal M. M., Nakar U., Singer L. e. a., 2017, *Science*, 358, 1559
 Lattimer J. M., Schramm D. N., 1974, *ApJ*, 192, L145
 Liu X., Osher S., 1998, *J. Comput. Phys.*, 142, 304
 MacFadyen A. I., Ramirez-Ruiz E., Zhang W., 2005, *astro-ph/0510192*,
 Margalit B., Metzger B., 2017, preprint ([arXiv:1710.05938](https://arxiv.org/abs/1710.05938))
 Margalit B., Metzger B. D., Beloborodov A. M., 2015, *Phys. Rev. Lett.*, 115, 171101
 Margutti R., et al., 2018, *ApJL*, 856, L18
 Michel F. C., Dessler A. J., 1981, *ApJ*, 251, 654
 Mooley K. P., et al., 2018, *Nature*, 554, 207
 Nakar E., Gottlieb O., Piran T., Kasliwal M. M., Hallinan G., 2018, preprint, ([arXiv:1803.07595](https://arxiv.org/abs/1803.07595))
 Paczynski B., 1986, *Astrophys. J.*, 308, L43
 Pili A. G., Bucciantini N., Del Zanna L., 2014, *MNRAS*, 439, 3541
 Read J. S., Lackey B. D., Owen B. J., Friedman J. L., 2009, *Phys. Rev.*, D79, 124032
 Reisswig C., Haas R., Ott C., Abdikamalov E., Mösta P., et al., 2013, *Phys.Rev.*, D87, 064023
 Rezzolla L., Kumar P., 2015, *Astrophys. J.*, 802, 95
 Rezzolla L., Most E. R., Weih L. R., 2017, preprint ([arXiv:1711.00314](https://arxiv.org/abs/1711.00314))
 Rosswog S., Davies M. B., 2002, *MNRAS*, 334, 481
 Rosswog S., Liebendörfer M., Thielemann F.-K., Davies M., Benz W., Piran T., 1999, *A & A*, 341, 499
 Rosswog S., Sollerman J., Feindt U., Goobar A., Korobkin O., Fremling C., Kasliwal M., 2017, preprint ([arXiv:1710.05445](https://arxiv.org/abs/1710.05445))
 Rowlinson A., O'Brien P. T., Metzger B. D., Tanvir N. R., Levan A. J., 2013, *MNRAS*, 430, 1061
 Ruiz M., Shapiro S. L., Tsokaros A., 2017, preprint ([arXiv:1711.00473](https://arxiv.org/abs/1711.00473))
 Shapiro S. L., 2000, *ApJ*, 544, 397
 Shapiro S. L., 2004, *ApJ*, 610, 913
 Shibata M., Fujibayashi S., Hotokezaka K., Kiuchi K., Kyutoku K., Sekiguchi Y., Tanaka M., 2017, preprint ([arXiv:1710.07579](https://arxiv.org/abs/1710.07579))
 Shu C., Osher S., 1989, *J. Comput. Phys.*, 83, 32
 Smartt S. J., et al., 2017, *Nature*
 Stark R. F., Piran T., 1987, *Computer Physics Reports*, 5, 221

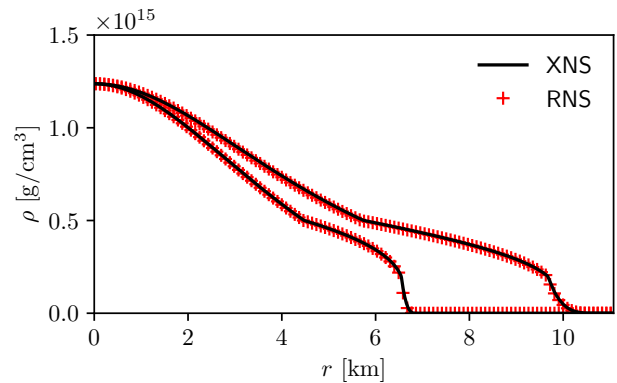


Figure A1. Comparison between XNS (black lines) and RNS (red crosses) of the rest mass density radial profiles along the equatorial and polar axes.

Stergioulas N., Friedman J. L., <http://www.gravity.phys.uwm.edu/rns/>
 Stergioulas N., Friedman J. L., 1995, *Astrophys. J.*, 444, 306
 Tanvir N. R., et al., 2017, *Astrophys. J.*, 848, L27
 Thierfelder M., Bernuzzi S., Hilditch D., Brüggmann B., Rezzolla L., 2011a, *Phys.Rev.*, D83, 064022
 Thierfelder M., Bernuzzi S., Brüggmann B., 2011b, *Phys.Rev.*, D84, 044012
 Villaseñor J. S., et al., 2005, *Nature*, 437, 855
 Wang Z., 2014, *Planet. Space Sci.*, 100, 19
 Wang Z., Chakrabarty D., Kaplan D. L., 2006, *Nature*, 440, 772
 Zeldovich Y. B., Novikov I. D., 1971, *Relativistic astrophysics. Vol.1: Stars and relativity*
 van Meter J. R., Baker J. G., Koppitz M., Choi D.-I., 2006, *Phys. Rev.*, D73, 124011

APPENDIX A: XNS CONVERGENCE

In this appendix we study the convergence of XNS and compare its results with the RNS code (Stergioulas & Friedman Stergioulas & Friedman, 1995). Since we are discussing code technical details, we will use code units, which are $c = G = M_{\odot} = 1$.

For this purpose, we adopt the same piecewise polytropic EOS of Case B, namely $p_1 = 10^{34.8}$ dyne/cm³ and $\Gamma_2 = 2.0$, and choose a model very close to the marginally stable Keplerian configuration. This is a quite demanding test, since the EOS is not a simple 1-piece polytropic and the model is very close to mass shedding.

The settings of the RNS benchmark are:

- radial grid points SDIV = 3601,
- angular grid points MDIV = 1201,
- polynomial expansion LMAX = 36,
- relative accuracy = 10^{-11} ,
- EOS recovered from interpolation of a 2000 point table.

The setting of the XNS configuration, which we will call “baseline” model, are the following:

- radial grid points NR = 2000,
- angular grid points NTH = 51,
- harmonic expansion MLS = 30,
- absolute convergence = 10^{-9} (cf. condition (iii) in Sec. 2.2),

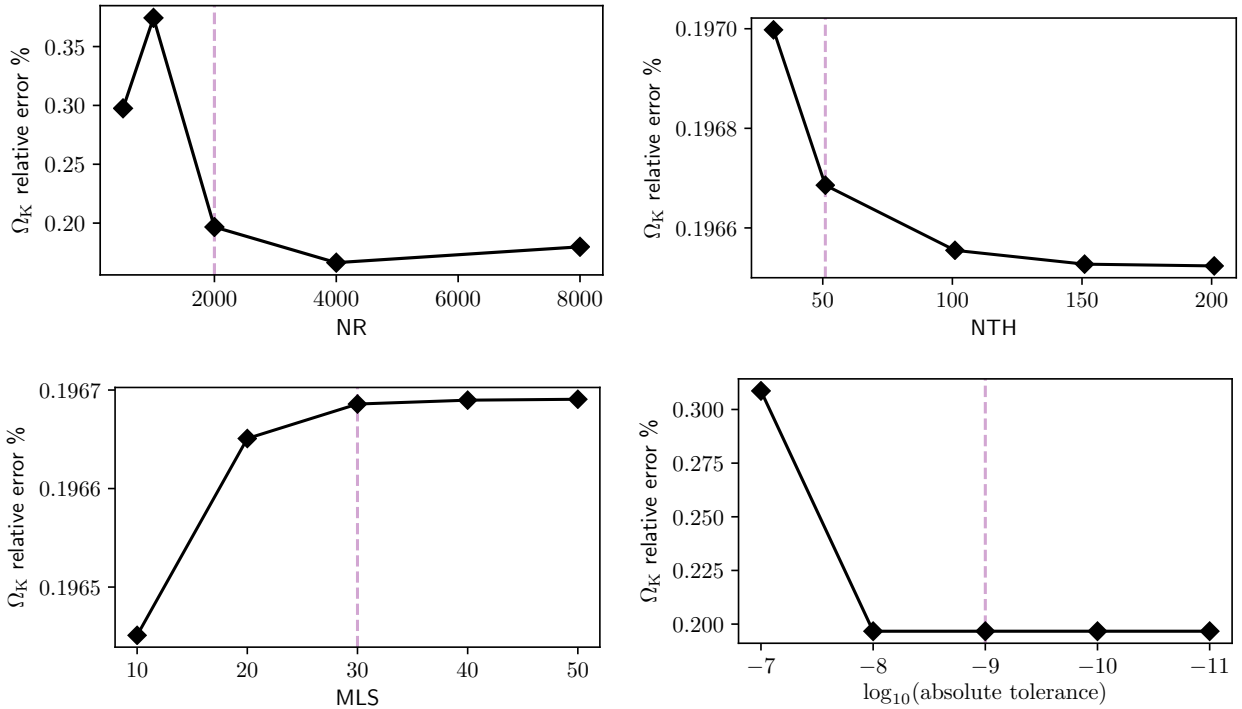


Figure A2. Convergence of the Keplerian angular velocity Ω_K obtained with XNS. We plot the relative error in percentage between the RNS benchmark and the XNS result, varying one XNS setting every time with respect to the baseline XNS model. From left to right and from top to bottom, we vary respectively the dimension of the radial grid NR, the dimension of the angular grid NTH, the number of components in the spherical harmonics expansion MLS, and the absolute tolerance criterion for convergence. The dashed, purple, vertical lines mark the settings of the XNS baseline model.

Table A1. Comparison in the model parameters in output from RNS and XNS. The columns contain: the stellar quantity, the RNS results, the XNS results, and the relative difference. The stellar quantities read from top to bottom: the gravitational mass M , the total angular momentum J , the angular speed Ω , the Keplerian angular speed Ω_K , the circumferential radius R , and the specific angular momentum at the equator j .

quantity	RNS	XNS	difference
M	2.6394	2.6382	0.05%
J	4.6745	4.6373	0.8%
Ω	0.040811	0.041000	0.5%
Ω_K	0.046103	0.046194	0.2%
R	10.668	10.596	0.7%
j	6.066	6.018	0.8%

- radius of the inner grid (which encompass half of the radial points) = 8,
- radius of the outer grid = 200.

The input parameters are the central density $\rho_c = 2.004 \times 10^{-3}$, and the angular speed $\Omega = 4.1 \times 10^{-2}$ for XNS and the aspect ratio $a = 0.61764727$ for RNS. We remark that the aspect ratio in output from the baseline XNS model is an input for the benchmark RNS model, and should therefore considered as “exact” for both codes.

In Tab. A1 we compare the output of the two codes and in Fig. A1 we compare the equatorial and polar density profiles. The range of the relative differences in the model

quantities between XNS and RNS is ~ 0.1 – 0.8% , except for the gravitational mass that is recovered within 0.05% . We remark that the extended conformal flatness approximation, on which XNS is based, neglects differences between the metric functions A and B of the order of $\sim 0.1\%$. Since the specific angular momentum at the ISCO of the equivalent Kerr black hole is $j_{\text{ISCO}} \simeq 7.0$ both for RNS and XNS, no debris disk is expected. This should not surprise since the configuration is close but not equal to the “Case B” described in the paper, for which we expect disk formation instead.

In Fig. A2 we plot the relative differences of the Keplerian angular velocity between the RNS benchmark and those obtained from the XNS model with the same settings of the XNS baseline model, apart for the setting that is varied in each plot. XNS shows a good convergence for each of the setting varied.

In conclusion, the comparison with RNS and the shown convergence validate the XNS code.

This paper has been typeset from a $\text{\TeX}/\text{\LaTeX}$ file prepared by the author.